INTERNATIONAL JOURNAL FOR NUMERICAL METHODS IN FLUIDS
Int. J. Numer. Meth. Fluids 2006; **52**:1005–1027
Published online 21 March 2006 in Wiley InterScience (www.interscience.wiley.com). DOI: 10.1002/fld.1219

A fractional two-step implicit algorithm using curvilinear collected grids

Jian Ye[1,*,†], J. A. McCorquodale[2,‡] and Jian Peng[3,§]

[1]*Managed-Programs LLC, 1880 Star-Batt Dr., Rochester Hills, MI 48309, U.S.A.*
[2]*Department of Civil and Environmental Engineering, University of New Orleans, New Orleans, LA 70148-2210, U.S.A.*
[3]*Department of Civil Engineering, University of Saskatchewan, Saskatoon, Saskatchewan, Canada, S7N 5A9*

SUMMARY

An efficient fractional two-step implicit algorithm is reported to simulate incompressible fluid flows in a boundary-fitted curvilinear collocated grid system. Using the finite volume method, the convection terms are discretized by the high-accuracy Roe's scheme to minimize numerical diffusion. An implicitness coefficient Π is introduced to accelerate the rate of convergence. It is demonstrated that the proposed algorithm links the fractional step method to the pressure correction procedure, and the SIMPLEC method could be considered as a special case of the fractional two-step implicit algorithm (when $\Pi = 1$). The proposed algorithm is applicable to unsteady flows and steady flows. Three benchmark two-dimensional laminar flows are tested to evaluate the performance of the proposed algorithm. Performance is measured by sensitivity analyses of the efficiency, accuracy, grid density, grid skewness and Reynolds number on the solutions. Results show that the model is efficient and robust. Copyright © 2006 John Wiley & Sons, Ltd.

KEY WORDS: collocated grid; curvilinear coordinates; finite volume method; fractional step algorithm; two-dimensional laminar flow; Roe's scheme

1. INTRODUCTION

When solving fluid dynamic problems, CFD analysts always deal with the challenges of complex geometries, non-linear physics, solution stability and accuracy, and computation

*Correspondence to: Jian Ye, Managed-Programs LLC, 1880 Star-Batt Dr., Rochester Hills, MI 48309, U.S.A.
†E-mail: jianye@managed-programs.com
‡E-mail: jamce@jazz.uno.edu
§E-mail: jian.peng@usask.ca

Contract/grant sponsor: University of Windsor
Contract/grant sponsor: Natural Science and Engineering Research Council of Canada
Contract/grant sponsor: Managed-Programs LLC

Received 4 April 2005
Revised 4 February 2006
Accepted 6 February 2006

efficiency. With increasing computational capability, numerical experiments have been conducted in developing various CFD modelling technologies.

To handle complex geometries, the boundary-fitted curvilinear coordinate transformation is one of the techniques developed to improve the applicability of conventional finite difference and finite volume methods [1–3]. When adopting curvilinear coordinates, it is desirable to operate within a collocated grid system, which requires less memory and computational time, and makes programming more convenient [4–8]. However, collocated grids with simple linear interpolation of velocities at control volume faces introduce non-physical grid scale oscillations in the results [4]. This drawback can be overcome by a momentum interpolation method first introduced by Rhie *et al.* [5], and later modified by Peric *et al.* [6] and Majumdar [7].

Higher-order schemes are normally used to interpolate the convection fluxes in discretizing the convection–diffusion transport equations [4, 9]. However, conventional higher-order upwind schemes, such as the second-order upwind scheme, QUICK scheme [10], etc., may suffer from 'overshoot' and/or 'undershoot' problems in regions where steep gradients exist. This challenge has led numerical studies in constructing more stable, accurate and efficient monotonic schemes. Sweby [11] evaluated some advanced schemes in several one-dimensional flows, and Tamamidis and Assanis [12] compared the performance of some high-order schemes for a range of two-dimensional unsteady flows, i.e. van Leer's scheme, Roe's scheme [13] and Leonard's SHARP scheme, for a range of two-dimensional unsteady flows. Their conclusion was that the second-order upwind Roe's scheme was the most accurate and efficient scheme among their test cases for pure convection with discontinuity. Other studies on the applications and comparison of other high-order schemes can be found in References [14–16].

In the simulation of incompressible fluid flows, a special difficulty arises due to the lack of a governing equation for the pressure, which results in a weak velocity–pressure coupling. This problem can be overcome by several approaches. One of the most commonly used methods is the pressure correction procedure as SIMPLE-type algorithm [4, 17]. However, the extension of this technique to non-orthogonal curvilinear grids leads to a very complex pressure correction procedure [3, 18]. Variants of SIMPLE-like algorithm have been continuously developed, for example, in References [19, 20].

Another successful approach is the fractional step or the projection method [21, 22], which is often applied to a time-discretized form of the transport equation. The principle of this method is to split the numerical operators into simpler parts, then apply an individual treatment to each part according to the properties of these operators.

An efficient fractional two-step implicit algorithm was proposed by Ye and Dou [23] initially for simulation of two-dimensional incompressible flows in Cartesian coordinates with a staggered grid arrangement. This fractional two-step algorithm was later modified by Ye and McCorquodale [8] to derive a depth-averaged model.

More recently, this methodology was extended into a fractional three-step algorithm by Ye *et al.* [24–26] to develop a three-dimensional hydrodynamic model with boundary-fitted curvilinear coordinates in horizontal plane, and a σ-coordinate transformation in vertical plane. Applications of this three-dimensional model include the simulation of various free surface turbulent flows and mass transport [24–26].

The objectives of this study focus on the development and evaluation of the efficient fractional two-step solution procedure following the previous works [8, 23–26]. As to two-dimensional laminar incompressible flows, the fractional two-step implicit algorithm is constructed based on the principle of the fractional method of Benque *et al.* [21]. Performance

is measured by sensitivity analyses of the efficiency, accuracy, grid density, grid skewness and Reynolds number on the solutions.

Combined with high-accuracy Roe's scheme, the fractional two-step implicit algorithm has been modified for the computation of two-dimensional incompressible laminar flows in boundary-fitted curvilinear collocated grids. The finite volume method is employed to discretize the governing equations. Three benchmark cases are tested to study the performance of the proposed model.

2. GOVERNING EQUATIONS

In (x, y) Cartesian coordinates, the governing equations for general two-dimensional laminar flows of an incompressible Newtonian fluid can be written as follows:

Continuity equation:

$$\frac{\partial u}{\partial x} + \frac{\partial v}{\partial y} = 0 \tag{1}$$

Momentum equations:

$$\frac{\partial \phi}{\partial t} + \frac{\partial u\phi}{\partial x} + \frac{\partial v\phi}{\partial y} = \frac{\partial}{\partial x}\left(v\frac{\partial \phi}{\partial x}\right) + \frac{\partial}{\partial y}\left(v\frac{\partial \phi}{\partial y}\right) + S_\phi \tag{2}$$

where

$$\phi = u, \quad S_u = -\frac{\partial p}{\partial x} \tag{3a}$$

$$\phi = v, \quad S_v = -\frac{\partial p}{\partial y} \tag{3b}$$

Equation (3a) applies to the x-momentum equation, while Equation (3b) is for the y-momentum equation. In these equations, u, v are the velocity components in the x, y, directions, respectively, v is the fluid kinematics viscosity, t is time and p is the kinetic pressure (pressure divided by the fluid density ρ). For simplification, a constant density is used here to illustrate the derivation of the algorithm.

Boundary-fitted coordinates (ξ, η) are introduced to represent the natural irregular geometry: $\xi = \xi(x, y)$, $\eta = \eta(x, y)$. In the new coordinate system, the velocities are defined as

$$U = uy_\eta - vx_\eta, \quad V = vx_\xi - uy_\xi \tag{4}$$

where U, V are called the contravariant velocities which are perpendicular to the η, ξ curvilinear coordinates, respectively.

The Cartesian velocity components (represented by φ) are used as dependent variables so that the momentum equations remain in a relatively simple conservative form [2]. Using the chain rule, the governing equations in non-orthogonal curvilinear coordinates can be stated as follows.

Continuity equation:

$$\frac{\partial U}{\partial \xi} + \frac{\partial V}{\partial \eta} = 0 \tag{5}$$

Momentum equations:

$$\frac{\partial J\phi}{\partial t} + \frac{\partial U\phi}{\partial \xi} + \frac{\partial V\phi}{\partial \eta} = \frac{\partial}{\partial \xi}\left[\frac{\nu}{J}(\alpha\phi_\xi - \beta\phi_\eta)\right] + \frac{\partial}{\partial \eta}\left[\frac{\nu}{J}(\gamma\phi_\eta - \beta\phi_\xi)\right] + S_\phi \tag{6}$$

where

$$\alpha = x_\eta^2 + y_\eta^2, \quad \beta = x_\xi x_\eta + y_\xi y_\eta, \quad \gamma = x_\xi^2 + y_\xi^2, \quad J = x_\xi y_\eta - x_\eta y_\xi \tag{7}$$

The source term S_φ is given by

$$S_u = -y_\eta \frac{\partial p}{\partial \xi} + y_\xi \frac{\partial p}{\partial \eta} \quad \text{when } \phi = u \tag{8}$$

$$S_v = -x_\xi \frac{\partial p}{\partial \eta} + x_\eta \frac{\partial p}{\partial \xi} \quad \text{when } \phi = v \tag{9}$$

3. NUMERICAL PROCEDURE

3.1. The fractional two-step implicit algorithm

Based on the fractional step approach of Benque *et al.* [21] for the different transport processes, the numerical procedure for the fractional two-step implicit algorithm proposed by Ye *et al.* [8, 23] is divided into the following two steps:

Step 1: Convection–diffusion process $\Rightarrow u^{n+1/2}, v^{n+1/2}$;
Step 2: Propagation process $\Rightarrow p^{n+1}, u^{n+1}, v^{n+1}$.

In this procedure, the superscript $n+1$ refers to the time level $(n+1)\Delta t$, etc., while the superscript $n+1/2$ is symbolic of the intermediate variables between steps. Define, for convenience, the following primed quantities: $[(u,v)=(u_1,u_2),(U,V)=(U_1,U_2)]$

$$u_{i'} = u_i^{n+1} - u_i^{n+1/2}, \quad U_{i'} = U_i^{n+1} - U_i^{n+1/2}, \quad p' = p^{n+1} - p^n, \quad (i=1,2) \tag{10}$$

In the propagation step, a coefficient of implicitness Π is introduced for spatial derivatives to accelerate the rate of convergence [8, 23], e.g. for ξ direction,

$$\begin{aligned} \frac{\partial p}{\partial \xi} &= \Pi\left(\frac{\partial p}{\partial \xi}\right)^{n+1} + (1-\Pi)\left(\frac{\partial p}{\partial \xi}\right)^{n} = \left(\frac{\partial p}{\partial \xi}\right)^{n} + \Pi\frac{\partial p'}{\partial \xi} \\ \frac{\partial U_j}{\partial \xi} &= \Pi\left(\frac{\partial U_j}{\partial \xi}\right)^{n+1} + (1-\Pi)\left(\frac{\partial U_j}{\partial \xi}\right)^{n+1/2} = \left(\frac{\partial U_j}{\partial \xi}\right)^{n+1/2} + \Pi\frac{\partial U_{j'}}{\partial \xi} \end{aligned} \tag{11}$$

In application, the known values of the pressure gradient in the momentum equations at the time level $n\Delta t$ are solved explicitly in Step 1 as source terms; the remainder of which, i.e.

$\partial p'/\partial\xi$ term, combined with the continuity equations are evaluated in Step 2 [8, 23]. Thus, the working equations of this fractional step algorithm are:

Step 1: Convection–diffusion process

$$J\frac{\phi^{n+1/2}-\phi^n}{\Delta t}+[U^n\phi^{n+1/2}]_\xi+[V^n\phi^{n+1/2}]_\eta$$
$$=\left[\frac{\nu}{J}(\alpha\phi_\xi^{n+1/2}-\beta\phi_\eta^n)\right]_\xi+\left[\frac{\nu}{J}(\gamma\phi_\eta^{n+1/2}-\beta\phi_\xi^n)\right]_\eta+S_\phi^n \tag{12}$$

where

$$\phi=u,\quad S_u^n=-y_\eta\frac{\partial p^n}{\partial\xi}+y_\xi\frac{\partial p^n}{\partial\eta}\quad\text{and}\quad\phi=v,\quad S_v^n=-x_\xi\frac{\partial p^n}{\partial\eta}+x_\eta\frac{\partial p^n}{\partial\xi}$$

Step 2: Propagation process

$$J\frac{u^{n+1}-u^{n+1/2}}{\Delta t}=-\Pi\left(\frac{\partial p'}{\partial\xi}y_\eta-\frac{\partial p'}{\partial\eta}y_\xi\right) \tag{13a}$$

$$J\frac{v^{n+1}-v^{n+1/2}}{\Delta t}=-\Pi\left(\frac{\partial p'}{\partial\eta}x_\xi-\frac{\partial p'}{\partial\xi}x_\eta\right) \tag{13b}$$

$$\frac{\partial U^{n+1/2}}{\partial\xi}+\frac{\partial V^{n+1/2}}{\partial\eta}+\Pi\left(\frac{\partial U'}{\partial\xi}+\frac{\partial V'}{\partial\eta}\right)=0 \tag{13c}$$

3.2. Numerical discretization

The working equations of each step are discretized using the control-volume-based finite difference method. The notation of Patankar [4] has been adopted throughout the following derivation. A typical control volume for node P is shown in Figure 1, where the capital letters E, N, etc. denote the neighbouring nodes and the lower case letters e, n, etc. denote the control volume faces.

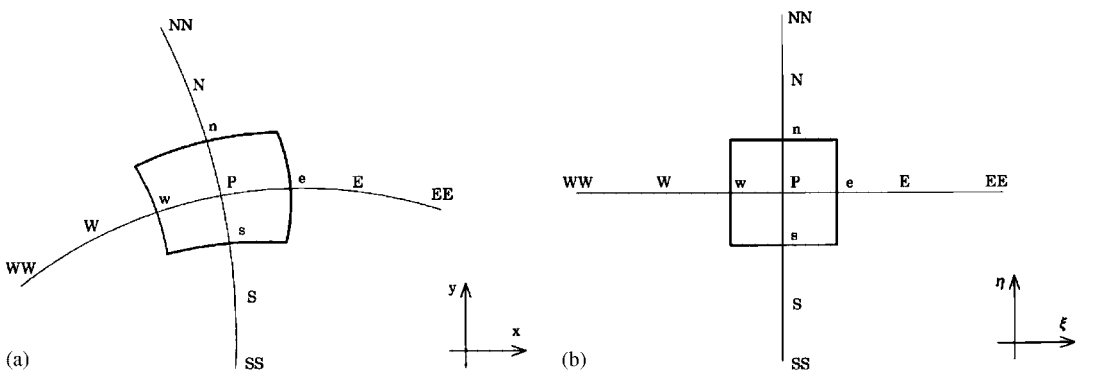

Figure 1. Control volume in: (a) physical; and (b) computational planes.

In Step 1, the general form of convection–diffusion equation (12) is integrated over a typical control volume of node P. All spatial derivatives are approximated with central differences of second-order accuracy, except for the convection terms whose face values can be represented in terms of nodal values by a variety of upwind schemes. To minimize the numerical diffusion, this paper employs Roe's scheme [13] in interpolating of convective fluxes because of its good performance in shock-capture and its high computational efficiency.

Based on an approximate Riemann solver, Roe [13] constructed a conservative upwind monotonic scheme of second-order accuracy. Sweby [11] converted Roe's transfer function to a flux limiter, e.g. in a uniform grid system at face e, the convection flux $U\Phi$ is written as [11, 12]:

$$(U\phi)_{\mathrm{e}} = [F_{\mathrm{e}}, 0](\phi_P + \Omega_{\mathrm{e}}^{-}\Delta\phi_{\mathrm{e}}^{-}) - [-F_{\mathrm{e}}, 0](\phi_{\mathrm{E}} - \Omega_{\mathrm{e}}^{+}\Delta\phi_{\mathrm{e}}^{+}) \tag{14}$$

where

$$\Delta\phi_{\mathrm{e}}^{-} = (\phi_P - \phi_{\mathrm{W}}) * 0.5; \quad \Delta\phi_{\mathrm{e}}^{+} = (\phi_{\mathrm{EE}} - \phi_{\mathrm{E}}) * 0.5 \tag{15}$$

$$\Omega_{\mathrm{e}}^{\pm} = [0, \min(2r_{\mathrm{e}}^{\pm}, 1), \min(r_{\mathrm{e}}^{\pm}, 2)] \tag{16}$$

$$r_{\mathrm{e}}^{-} = (\phi_{\mathrm{E}} - \phi_P)/(\phi_P - \phi_{\mathrm{W}}); \quad r_{\mathrm{e}}^{+} = (\phi_P - \phi_{\mathrm{E}})/(\phi_{\mathrm{E}} - \phi_{\mathrm{EE}}) \tag{17}$$

Here $F_{\mathrm{e}} = U_{\mathrm{e}}$, r_{e} is the ratio of consecutive gradients, and Ω_{e} is the flux limiter which corresponds to Roe's 'superbee' compressive transfer function. The term $F_{\mathrm{e}}\Omega_{\mathrm{e}}\Delta\varphi_{\mathrm{e}}$ is a form of high-order-limited antidiffusion flux, and the resulting scheme is monotonic and ensures oscillation-free solutions.

The final discretized form of Equation (12), with $\Delta\xi = \Delta\eta = 1$, is

$$a_P\phi_P^{n+1/2} = \Sigma a_{nb}\phi_{nb}^{n+1/2} + b + a_P^{*}\phi_P^{n} + S_\phi \tag{18}$$

The coefficients of Equation (18) can be written in the following compact format:

$$a_{\mathrm{E}} = D_{\mathrm{e}}A(|P_{\mathrm{e}}|) + [-F_{\mathrm{e}}, 0], \quad a_{\mathrm{W}} = D_{\mathrm{w}}A(|P_{\mathrm{w}}|) + [F_{\mathrm{w}}, 0]$$

$$a_{\mathrm{N}} = D_{\mathrm{n}}A(|P_{\mathrm{n}}|) + [-F_{\mathrm{n}}, 0], \quad a_{\mathrm{S}} = D_{\mathrm{s}}A(|P_{\mathrm{s}}|) + [F_{\mathrm{s}}, 0]$$

$$a_P = \Sigma a_{nb} + a_P^{*}, \quad a_P^{*} = J/\Delta t, \quad P_i = F_i/D_i$$

$$F_{\mathrm{e}} = U_{\mathrm{e}}^{n}, \quad F_{\mathrm{w}} = U_{\mathrm{w}}^{n}, \quad D_{\mathrm{e}} = (\alpha v/J)_{\mathrm{e}}/\delta\xi_{\mathrm{e}}, \quad D_{\mathrm{w}} = (\alpha v/J)_{\mathrm{w}}/\delta\xi_{\mathrm{w}}$$

$$F_{\mathrm{n}} = V_{\mathrm{n}}^{n}, \quad F_{\mathrm{s}} = V_{\mathrm{s}}^{n}, \quad D_{\mathrm{n}} = (\gamma v/J)_{\mathrm{n}}/\delta\eta_{\mathrm{n}}, \quad D_{\mathrm{s}} = (\gamma v/J)_{\mathrm{s}}/\delta\eta_{\mathrm{s}}$$

$$b = -\left(\frac{v}{J}\beta\phi_\eta^{n}\right)\Big|_{\mathrm{w}}^{e} - \left(\frac{v}{J}\beta\phi_\xi^{n}\right)\Big|_{\mathrm{s}}^{n} + B_{\mathrm{anti}}$$

where

$$A(|P|) \equiv 1$$

$$\begin{aligned} B_{\mathrm{anti}} = {} & [F_{\mathrm{w}}, 0]\Omega_{\mathrm{w}}^{-}\Delta\phi_{\mathrm{w}}^{-} + [-F_{\mathrm{w}}, 0]\Omega_{\mathrm{w}}^{+}\Delta\phi_{\mathrm{w}}^{+} - [F_{\mathrm{e}}, 0]\Omega_{\mathrm{e}}^{-}\Delta\phi_{\mathrm{e}}^{-} - [-F_{\mathrm{e}}, 0]\Omega_{\mathrm{e}}^{+}\Delta\phi_{\mathrm{e}}^{+} \\ & + [F_{\mathrm{s}}, 0]\Omega_{\mathrm{s}}^{-}\Delta\phi_{s}^{-} + [-F_{\mathrm{s}}, 0]\Omega_{\mathrm{s}}^{+}\Delta\phi_{\mathrm{s}}^{+} - [F_{\mathrm{n}}, 0]\Omega_{\mathrm{n}}^{-}\Delta\phi_{\mathrm{n}}^{-} - [-F_{\mathrm{n}}, 0]\Omega_{\mathrm{n}}^{+}\Delta\phi_{\mathrm{n}}^{+} \end{aligned} \tag{19}$$

In two-dimensional computations, Roe's flux-limiting scheme is a 9-point stencil and is conservative.

Other schemes can be incorporated easily in the code. For example, the Power-law scheme [4] will be constructed, if Equation (19) is replaced by the following Equation (20).

$$A(|P|) = [0, (1 - 0.1|P|)^5], \quad B_{\text{anti}} \equiv 0 \tag{20}$$

Thus, the equations in Step 1 are discretized as follows.

u-momentum equation

$$a_P u_P^{n+1/2} = \Sigma a_{nb} u_{nb}^{n+1/2} + b^u + a_P^* u_P^n + B^u \frac{\partial p^n}{\partial \xi} + C^u \frac{\partial p^n}{\partial \eta} \quad \text{where } B^u = -y_\eta, C^u = y_\xi \tag{21}$$

v-momentum equation

$$a_P v_P^{n+1/2} = \Sigma a_{nb} v_{nb}^{n+1/2} + b^v + a_P^* v_P^n + B^v \frac{\partial p^n}{\partial \xi} + C^v \frac{\partial p^n}{\partial \eta} \quad \text{where } B^v = x_\eta,\ C^v = -x_\xi \tag{22}$$

In Step 2, from Equations (13a) and (13b), one obtains u', v' as

$$u' = -d\left(\frac{\partial p'}{\partial \xi} y_\eta - \frac{\partial p'}{\partial \eta} y_\xi\right), \quad v' = -d\left(\frac{\partial p'}{\partial \eta} x_\xi - \frac{\partial p'}{\partial \xi} x_\eta\right) \tag{23}$$

then,

$$U' = u' y_\eta - v' x_\eta = -B\frac{\partial p'}{\partial \xi} + \beta d \frac{\partial p'}{\partial \eta} \tag{24}$$

$$V' = v' x_\xi - u' y_\xi = -C\frac{\partial p'}{\partial \eta} + \beta d \frac{\partial p'}{\partial \xi} \quad \text{where } d = \Pi \Delta t / J,\ B = \alpha d, C = \gamma d \tag{25}$$

The above relations can be applied to any location, that is, at either a grid node or control volume face. To simplify the pressure correction equation and keep the 5-point diagonal equation set, the last term on the right-hand side of Equations (24) and (25) can be dropped without affecting the final converged results. Thus,

$$U' \approx -B\frac{\partial p'}{\partial \xi}, \quad V' \approx -C\frac{\partial p'}{\partial \eta} \tag{26}$$

Substituting Equation (26) into Equation (13c), the final pressure correction equation is

$$A_P p_{P'} = \Sigma A_{nb} p_{n'b} + E \tag{27}$$

where

$$A_{\text{E}} = \Pi B_{\text{e}}, \quad A_{\text{W}} = \Pi B_{\text{w}}, \quad A_{\text{N}} = \Pi C_{\text{n}}, \quad A_{\text{S}} = \Pi C_{\text{s}}$$

$$A_P = \Sigma A_{nb}, \quad E = U^{n+1/2}\big|_{\text{e}}^{w} + V^{n+1/2}\big|_{\text{n}}^{s}$$

In Step 2, the pressure propagation process of the proposed algorithm resembles the velocity–pressure correction procedure in the SIMPLE-like algorithm. In comparison to the

corresponding process of the SIMPLEC algorithm [17, 18] in non-orthogonal curvilinear grids, it is obvious that the derivation of the velocity and pressure correction equations (23), (26) and (27) is much simpler and straightforward. In fact, when $\Pi = 1$, these velocity and pressure correction equations become those derived by the SIMPLEC algorithm [17, 18, 23]. Thus, the SIMPLEC method could be considered as a special case of the current proposed fractional step method. In other words, the proposed fractional two-step implicit algorithm links the fractional method and the pressure correction procedure together. Similar conclusions can be found in References [8, 23].

3.3. Pressure–velocity coupling

Since collocated grids having been adopted, all the dependent variables are stored at the grid nodes and interpolation is needed to estimate the convective flux at the control volume faces, e.g. $U_{\mathrm{e}}^{n+1/2}, V_{\mathrm{n}}^{n+1/2}$, in the source term E of Equation (27). To avoid checkerboard oscillatory solutions caused by simple linear interpolation between the neighbouring nodal values [4], the revised momentum interpolation procedure of Majumdar [7] is used since the converged solution of this method is independent of the relaxation parameter (or time step Δt in the unsteady approach). The values of U at the e cell face can be expressed as

$$U_{\mathrm{e}}^{n+1/2} = \langle \overline{U_P^{n+1/2}} \rangle_{\mathrm{e}} + \left\langle \overline{\frac{a_p^*}{a_P}} \right\rangle_{\mathrm{e}} U_{\mathrm{e}}^n - \left\langle \overline{\frac{a_p^*}{a_P} U_P^n} \right\rangle_{\mathrm{e}} + \left\langle \overline{\frac{B^u}{a_P} y_\eta - \frac{B^v}{a_P} x_\eta} \right\rangle_{\mathrm{e}} \left(\frac{\partial p^n}{\partial \xi} \right)_{\mathrm{e}} - \left\langle \overline{\left(\frac{B^u}{a_P} y_\eta - \frac{B^v}{a_P} x_\eta \right) \left(\frac{\partial p^n}{\partial \xi} \right)_P} \right\rangle_{\mathrm{e}} \tag{28}$$

where the overbars denote the control volume face values estimated by linear interpolation between the neighbouring nodal values. The expressions of B^u, B^v, etc. are given in Equations (21) and (22). The contravariant velocity V at the north cell face can be expressed similarly.

3.4. Solution procedure

The overall numerical procedure of the proposed two-step implicit fractional step algorithm can be summarized as follows:

1. the known values of u^n, v^n, p^n at time $n\Delta t$ are used to evaluate the coefficients of the convection–diffusion Equation (12) and obtain velocities $u^{n+1/2}$, $v^{n+1/2}$ through Equations (21) and (22) at the grid nodes to complete Step 1.
2. interpolate $U^{n+1/2}, V^{n+1/2}$, etc. onto the cell faces.
3. solve Equation (27) for p' and p^{n+1}, then obtain U^{n+1}, V^{n+1} according to Equations (26) and (10) to complete Step 2.
4. solve the discretized transport equations for other scalar variables to finish the current time step (no other transport equation is to be solved here).
5. return to 1 and march to the next time step.
6. repeat the whole procedure until a steady-state solution is reached (for steady-state flow) or the specified time period is completed (for unsteady flow).

As derivation procedure showed above, the proposed algorithm is applicable to both unsteady and steady flows. In the present study of stead flows, the time-marching scheme is used as a technique to obtain a steady-state solution as a limiting case. The algebraic equation sets are solved sequentially using the familiar tridiagonal matrix algorithm (TDMA) on a grid line. The convergence criterion adopted is that the non-dimensional total mass residuals (R) be less than a certain value. The typical value of the implicitness coefficient Π is in the range of 0.5–1. As shown by Ye *et al.* [22], the rate of convergence can be significantly accelerated by reducing Π from 1 to its optimal value.

4. NUMERICAL RESULTS AND DISCUSSION

Three two-dimensional test problems have been used to investigate the performance of the proposed numerical model. The three cases are (1) pure convection of a box-shaped profile, for model *verification* by comparison to an analytical solution; (2) laminar flow over a backward-facing step, for model *validation* by comparison to experimental data of Armaly *et al.* [27]; (3) skewed driven cavity laminar flow, *benchmarking* for 'code-to-code' comparison.

Case 1: Pure convection of a box-shaped profile

The first problem is the transport of φ (any scalar quantity) in a two-dimensional skewed constant flow field without physical diffusion effects. A discontinuous step profile ($\varphi = 1$ or $\varphi = 0$) is imposed along the left-hand and front upstream boundaries, as shown in Figure 2. Pure convection of φ is conducted in an oblique uniform flow field at an angle of 45° to the x-axis, and the discontinuity must be maintained downstream. This test problem was first selected by Gaskell and Lau [14] in their SMART scheme verification because the severe change in the gradient of φ is representative of many practical flow situations.

In a square domain with a uniform 41×41 grid ($\Delta x = \Delta y = 1$), Figures 2(a) and (b) show the prediction by Roe's and the first-order upwind scheme, respectively. The computations

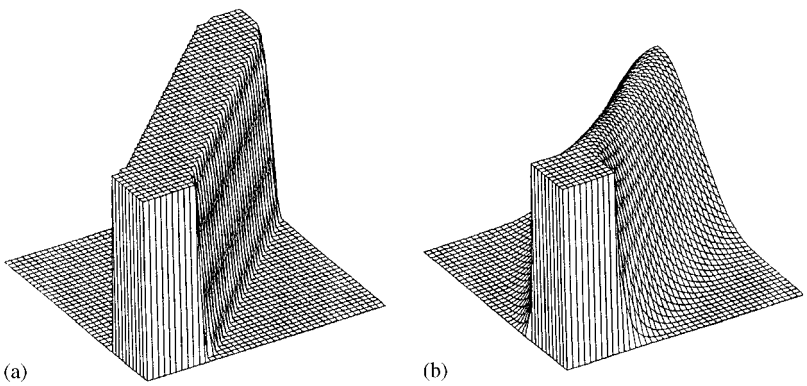

Figure 2. Pure convection of a box-shaped profile at 45° to the x-axis by: (a) Roe's scheme; and (b) first-order upwind scheme.

indicate that the poor performance of the first-order upwind scheme tends to smear the box-shaped profile due to the high numerical diffusion. For example, along the halfway cross section, i.e. $x = 20$, the maximum and minimum values of φ calculated by the first-order scheme are $\varphi_{max} = 0.89$ and $\varphi_{min} = 0.24 \times 10^{-3}$, respectively (as compared with the exact solutions $\varphi_{max} = 1$ and $\varphi_{min} = 0$). Roe's scheme, by contrast, exhibits an excellent performance in capturing the discontinuity of the steep gradient of φ. Along the halfway cross section, the maximum and minimum values of φ simulated by Roe's scheme are $\varphi_{max} = 1$ (no overshoot) and $\varphi_{min} = -0.11 \times 10^{-7}$ (nearly no undershoot), respectively.

This pure convection problem verifies that Roe's scheme is able to minimize the numerical dispersion without introducing significant over- and/or under-shooting.

Case 2: Laminar flow over a backward-facing step

Flow separation is of fundamental importance in fluid mechanics. One of the simplest flows modelling the separation–reattachment process is the backward-facing step flow due to a sudden change of the geometry. The laminar case of Armaly *et al.* [26] is considered here to study the performance of the proposed algorithm, including the convergence, stability, accuracy, grid sensitivity and non-orthogonality. The backward-facing step geometry has become a standard test problem for code validation [28], and systematic study of its numerical solutions can be found in References [28–31].

Figure 3 illustrates the flow past a backward-facing step. $x1$ is the reattachment location of the primary recirculation. $x2$ and $x3$ are the separation and reattachment points, respectively, of the secondary recirculation at the top wall. The expansion ratio of the inlet channel height h (here $h = 1$) to the outlet height is 1:2. The Reynolds number is defined as $Re = U_0 D/v$ using $2h$ as D and the mean u-velocity at the step as U_0. At low Reynolds numbers, a single recirculation zone appears behind the step. At higher Reynolds numbers, the adverse pressure gradient is strong enough to cause an upper separating zone, as shown in Figure 3. As long as the flow is laminar, the separation zones increase in size with increasing Reynolds number [27]. The reattachment length is a sensitive parameter often used to appraise the overall predictive capability of a numerical method. The recirculation zones reduce in length when numerical diffusion, arising from discretized convection terms, overwhelms the true viscosity of the flow. For higher Reynolds numbers ($Re > 400$), the three-dimensional flow structures affect the primary separation–reattachment across the floor of the downstream channel, and

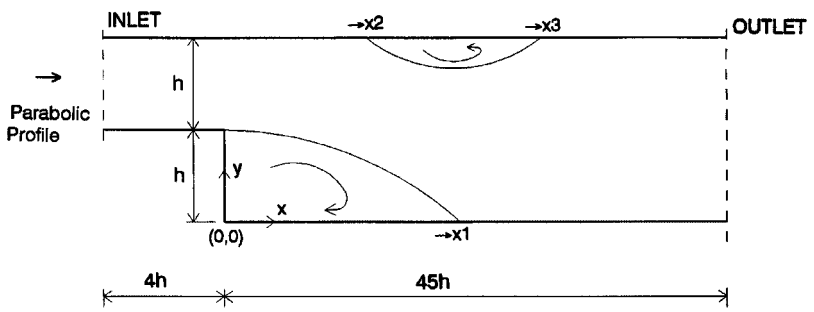

Figure 3. Laminar flow past a backward-facing step.

two-dimensional models can exhibit certain disagreement between the numerical and experimental results [27, 28].

The boundary conditions include no-slip velocity specification at all solid walls and prescribed fully developed laminar parabolic velocity profile at the inlet, situated at a distance $4h$ upstream of the step. The outlet boundary is set far downstream from the step so that the flow leaves the domain of interest without perturbing the upstream flow. Across the outlet, a parallel flow (Neumann condition) is prescribed and the pressure is set to zero. Previous studies have suggested $32h$ downstream of the step as the appropriate location of the outlet [30, 32, 33]. The sensitivity of the solution to the location of the outlet boundary conditions was investigated numerically by Gartling [29] for the case of Armaly *et al.* [27] at $Re = 800$. This study indicated that the length of $32h$ would not be sufficiently long for the constant pressure assumption at the outlet. The downstream channel length was taken as $60h$ at $Re = 800$ in Gartling's study. In the present work with $Re = 600$, the outlet is located at $45h$ downstream of the step, providing both reasonable accuracy and economics.

The computations have been carried out on three non-uniformly distributed grids, namely, 90×20 (coarse) grid, 260×40 (fine) grid and 350×80 (very fine) grid. The Reynolds numbers selected are $Re = 100$, 200, 300, 400, 500, 600. The convergence criterion is that the non-dimensional total mass residuals R reduce to less than 10^{-5}. The recirculation parameters $x1, x2, x3$ are determined by interpolation using longitudinal velocity data at the locations near the reattachment and separation positions.

Grid dependence (refinement) and numerical diffusion

Reattachment and separation lengths from the finest grid are considered as the grid-independent results. Comparison with the data of Armaly *et al.* [27] is presented in Figure 4. For the primary reattachment length $x1$, agreement between the simulation and measurement is good at the lower Reynolds numbers ($Re < 400$); however, at the higher Reynolds number ($Re > 400$), the discrepancy increases with increasing Reynolds numbers because of three-dimensional effects as demonstrated by Williams and Baker [28]. The upper wall recirculation parameters $x2$, $x3$ are reasonably well predicted. These conclusions are consistent with others [28, 30, 32].

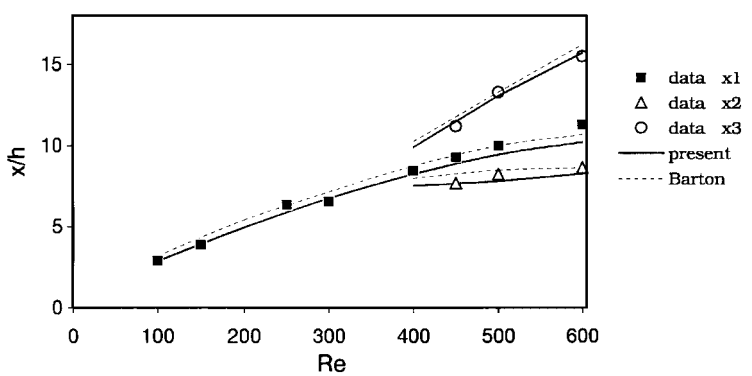

Figure 4. Comparison of the predicted reattachment and separation lengths with the measurement of Armaly *et al.* [27] and simulation of Barton [30].

Table I. Primary recirculation size $x1/h$ for various grids and (percentage difference) from the predicted grid-independent results for $Re = 100$ and 300.

Grid	$Re = 100$	$Re = 300$
90×20	2.83 (−1.5)	6.48 (−3.2)
260×40 (G1)	2.87 (−0.14)	6.65 (−0.6)
350×80	2.874 (0.0)	6.69 (0.0)

Table II. Separation lengths for various grids and (percentage difference) from the predicted grid-independent results for $Re = 500$.

Grid	$x1/h$	$x2/h$	$x3/h$
90×20	8.54 (−8.5)	6.94 (−11.1)	12.92 (−1.2)
260×40 (G1)	9.17 (−1.7)	7.62 (−2.4)	13.07 (−0.08)
350×80	9.33 (0.0)	7.81 (0.0)	13.08 (0.0)

The simulation results from an other high-accuracy scheme [30] are also shown in Figure 4 for comparison.

Generally, the reattachment and separation positions $(x1, x2, x3)$ grow with grid refinement. The primary recirculation zone $(x1)$ behind a backward-facing step becomes larger as the Reynolds number increases. Table I gives the results on the three grids for the flows in lower Reynolds numbers, i.e. $Re = 100$ and 300. Predictions from the fine grid approach the grid-independent results (relative variation around 1% is considered as close enough to be the same).

At higher Reynolds number, the upper recirculation zone is generated in addition to the primary recirculation zone. Performance of various grids and the percentage difference from the estimated grid-independent results are presented in Table II (for $Re = 500$), and Table III (for $Re = 600$). In the case of $Re = 500$, with the coarse grid, the results are considerable discrepancy for $x1$ and $x2$, while the prediction of $x3$ gives a reasonably good solution (with 1.2% underestimation). As the grid is refined, the solutions are improving. On the fine grid, it produces reasonably accurate solutions for $x1$ and $x3$. Because the upper separating region interacts with the primary recirculation zone, the separation position $x2$ is very sensitive and difficult to resolve. Considering this effect, the results from the fine grid are in good agreement with the grid-independent results from the finest grid.

The Power-law scheme is also tested in the same program code, just substituting Equation (19) by Equation (20). Results from $Re = 600$ are presented in Table III for comparison. It shows that the results from the Power-law scheme gives a much higher percentage change of the results as the grid is refined, and the reattachment and separation positions $(x1, x2, x3)$ are underestimated in all grids. Table III also indicates that even with the finest

Table III. Separation lengths for various grids and (percentage difference) from the predicted grid-independent results for $Re = 600$.

	$x1/h$		$x2/h$		$x3/h$	
Grid	Roe's	Power-law	Roe's	Power-law	Roe's	Power-law
90×20	9.15 (−10.2)	8.67 (−15.0)	7.1 (−14.3)	6.67 (19.4)	15.2 (−3.2)	11.5 (−26.8)
260×40	9.98 (−2.1)	9.48 (−7.1)	8.0 (−3.4)	7.46 (9.9)	15.6 (−0.6)	14.55 (−7.32)
350×80	10.2 (0.0)	9.85 (−3.4)	8.28 (0.0)	7.82 (−5.5)	15.7 (0.0)	15.15 (−3.5)

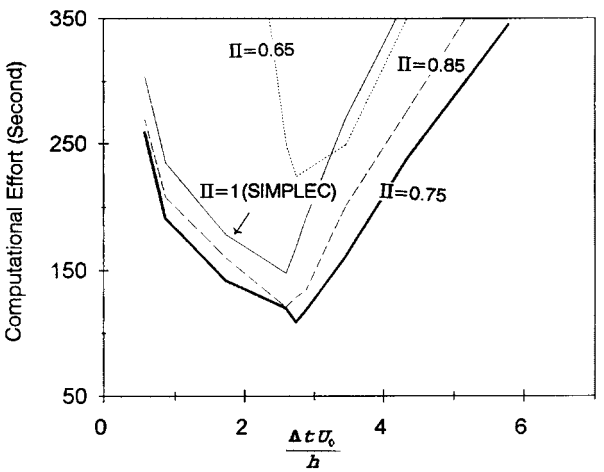

Figure 5. Computational effort with variation of Π for $Re = 100$.

mesh, the results from the Power-law scheme are still worse than that from Roe's scheme with the fine mesh. Similar solutions and conclusions were obtained by Barton [30] for the same problem at $Re = 600$ with the Hybrid scheme on a very fine 250×128 grid.

Convergence, stability and computation effort of the proposed algorithm

The performance of the proposed fractional two-step implicit algorithm is studied by varying the implicitness coefficient Π between 0.5 and 1, while $\Pi = 1$ corresponds to the SIMPLEC time-marching algorithm. Figures 5 and 6 illustrate the computational efforts for selected Π over a range of dimensionless time steps $\Delta t U_0/h$ on the coarse grid of 90×20. The results are driven to the same level of convergence ($R = 10^{-5}$). Figure 5 shows the case of $Re = 100$. The computational costs decrease continuously over a wider range of time step for convergence as Π reduces from 1.0 to 0.75; however, reduction of Π to 0.65 leads to higher computational

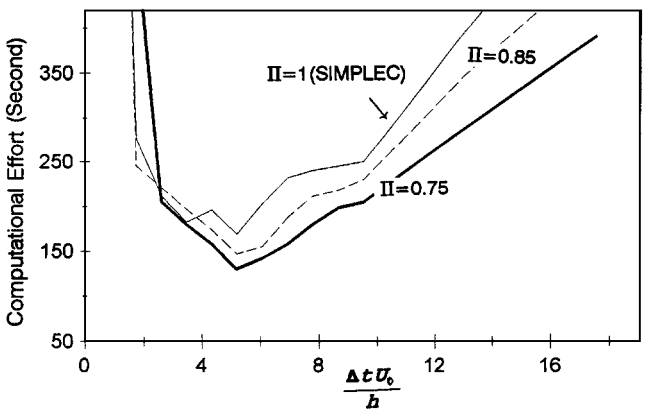

Figure 6. Computational effort with variation of Π for $Re = 300$.

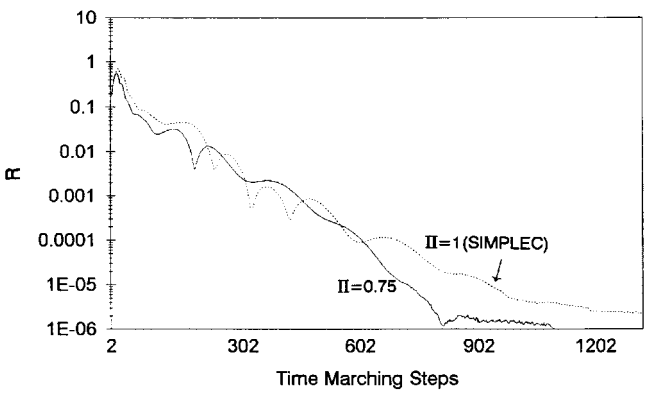

Figure 7. Convergence histories for $Re = 100$.

effort and a narrower range of convergence. Further reduction of Π may cause instability. This indicates that there exists an optimal value of Π and time step Δt. The computational effort saved in the optimal value of $\Pi = 0.75$ is about 30–40% in comparison with the SIMPLEC algorithm ($\Pi = 1$), depending on the time step. A similar conclusion can be drawn for flow at $Re = 300$, as demonstrated in Figure 6. Figures 7 and 8 depict the convergence histories against the time-marching steps for $\Pi = 0.75$ and 1 (SIMPLEC), and the Reynolds numbers $Re = 100$ and 300, respectively. The time steps are at their optimal values as shown in Figures 5 and 6. The convergence histories indicate the improvements achieved by the present algorithm.

Non-orthogonality of grids

The above computations were carried out in a rectangular grid system by taking advantage of the simple geometry of the problem. To evaluate the robustness of the code, it is desirable to

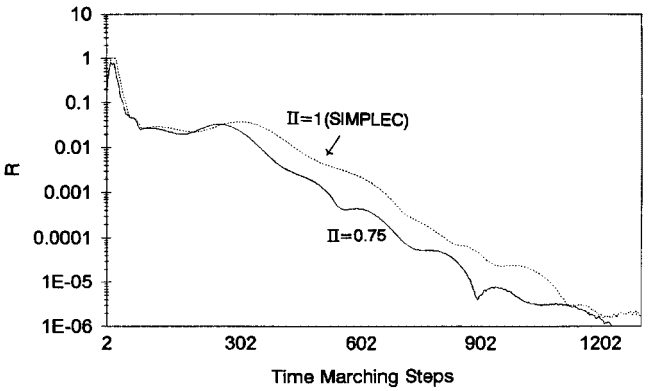

Figure 8. Convergence histories for $Re = 300$.

Table IV. Primary recirculation size $x1/h$ for non-orthogonal grids and (percentage difference) from the estimated grid-independent result for $Re = 300$.

Non-orthogonal grids (260×40)	$x1/h$
G2	6.67 (-0.3)
G3	6.66 (-0.45)

Table V. Separation lengths for non-orthogonal grids and (percentage difference) from the predicted grid-independent result for $Re = 500$.

Non-orthogonal grids (260×40)	$x1/h$	$x2/h$	$x3/h$
G2	9.23 (-1.1)	7.66 (-1.9)	13.03 (-0.38)
G3	9.16 (-1.8)	7.59 (-2.8)	13.19 ($+0.84$)

run it on non-orthogonal grids. Two non-orthogonal grids have been employed with density of 260×40, the same grid number as the fine rectangular grid (denoted as G1 hereafter). The non-orthogonal grids (denoted as G2 and G3) are designed to have a varying angle of $-35\,\mathrm{Exp}[-0.022(x/h-11)^2]$ and $-35\,\mathrm{Exp}[-0.022(x/h-11)^2]$ degrees, respectively, against the $x$axis at $y/h = 1$. The maximum skew grid (angle of 35°) is located at $x/h = 11$ around both recirculation regions in the higher Reynolds number flows. Results from the non-orthogonal $G2$ and $G3$ grids and the percentage difference from the estimated grid-independent results are presented in Table IV (for $Re = 300$), and Table V (for $Re = 500$). It is observed that the

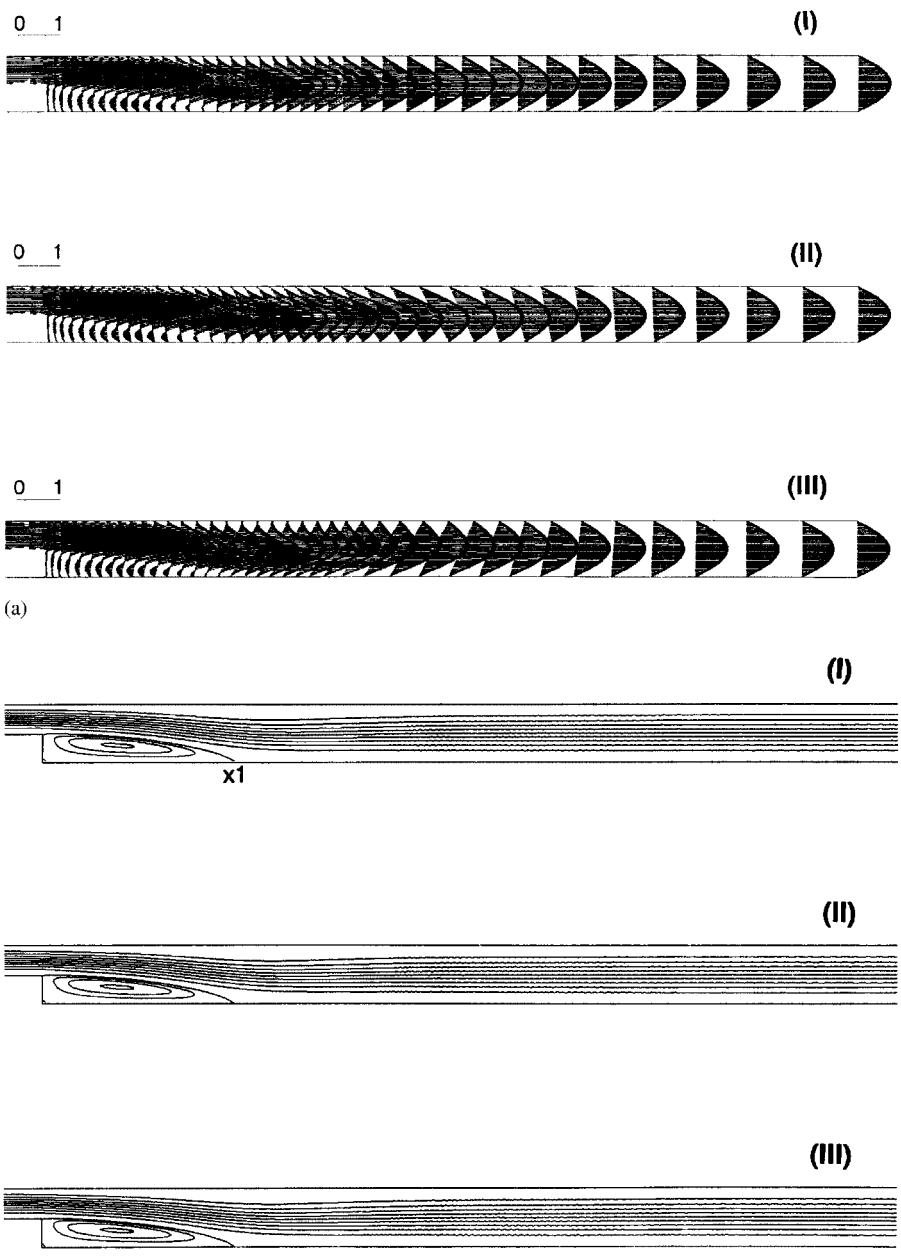

Figure 9. (a) Predicted velocity vector fields (non-dimensionalized by U_0) at $Re = 300$ for (I) G1, (II) G2, and (III) G3 grids; and (b) predicted streamlines at $Re = 300$ for (I) G1, (II) G2, and (III) G3 grids.

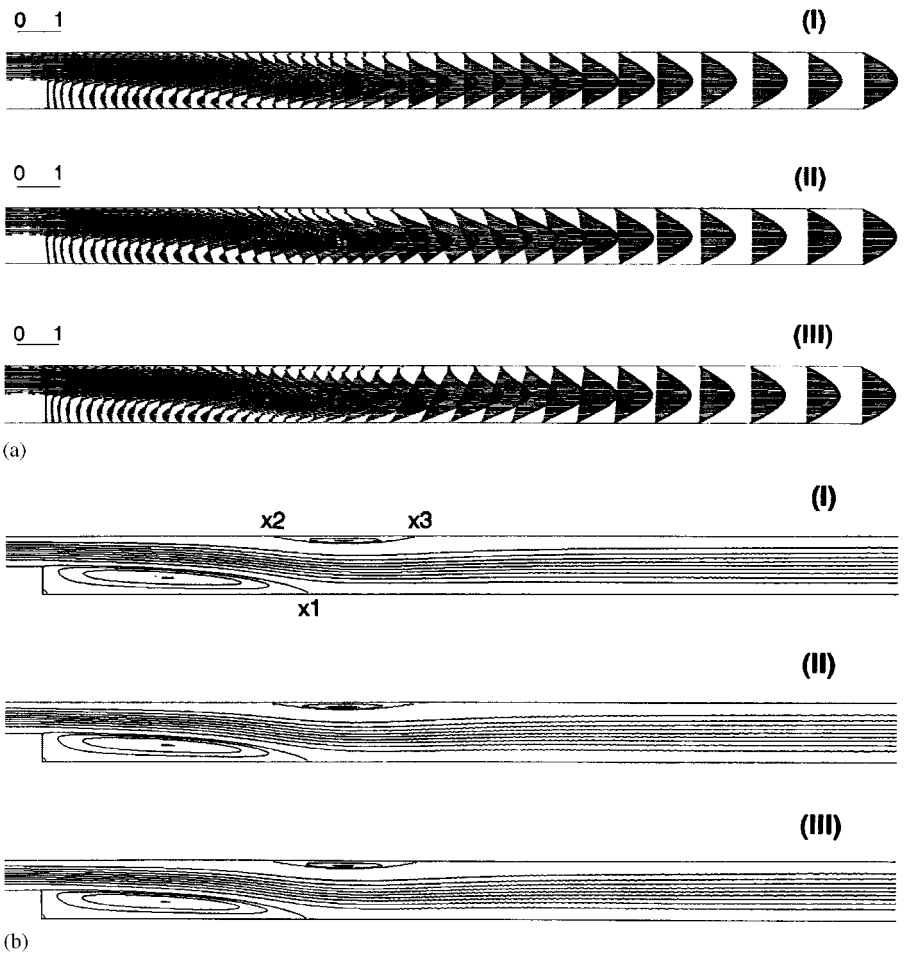

Figure 10. (a) Predicted velocity vector fields (non-dimensionalized by U_0) at $Re = 500$ for (I) G1, (II) G2 , and (III) G3 grids; and (b) predicted streamlines at $Re = 500$ for (I) G1, (II) G2, and (III) G3 grids.

relative variation of the results on the non-orthogonal grids is within 1% in comparison with the corresponding solutions on the rectangular G1 grid (Tables I and II), i.e. the characteristics of the recirculation regions in these three grids are virtually the same. Figures 9 and 10 present the velocity vector fields and streamline contours for $Re = 300$ and 500, respectively. Figures 9(a) and 10(a) also illustrate the grid distribution. The flow patterns on the three grids closely resemble each other.

Case 3: Skewed driven cavity laminar flow

Skewed driven cavity laminar flows were set up by Demirdzic *et al.* [34] for non-orthogonal grids as benchmark cases that have been computed by a number of researchers [31, 34–36]. The case with $\theta = 45°$ is considered here as shown in Figure 11 with two different Reynolds

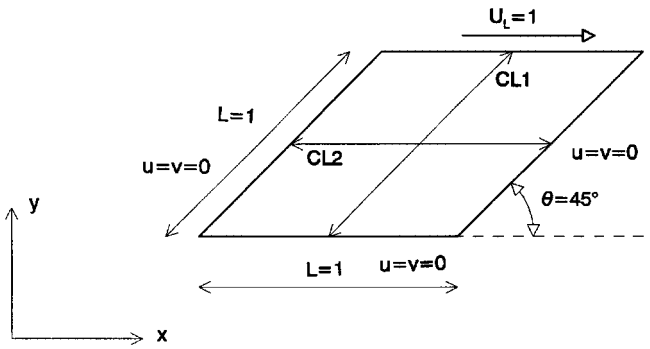

Figure 11. Geometry and boundary conditions for the skewed driven laminar cavity flow.

numbers, $Re = 100$ and 1000 ($Re = U_L L/v$). Experimental data are not available in literatures. The domain is a parallelogram of length $L = 1$, the velocity at the moving top wall is $U_L = 1$ and the velocities specified at the other three walls are zero. In the benchmark computations by Demirdzic *et al.* [34], six non-orthogonal grids were chosen with the computations on the finest 320×320 grid selected as the reference.

Three uniform non-orthogonal grids are selected to study the grid refinement effect, namely, the coarse 40×40 grid, the fine 80×80 grid, the finest 160×160 grid. The convergence criterion is that the total mass residuals R fall to less than 10^{-5}. The implicitness coefficient used is $\Pi = 0.75$.

The Cartesian velocity u and v profiles along the centrelines CL1 and CL2 are compared in Figures 12(a) and (b) with the benchmark solutions [34] for $Re = 100$. For the lower Reynolds number flow, it is remarkable that the results on all three grids are very close each other, and in excellent agreement with the benchmark computations.

Figures 13(a) and (b) illustrate the results for $Re = 1000$ on the three grids. As it is shown, accurate simulations of the velocities at the centrelines are obtained by the grid refined. In fact, on the finest grid, predictions from the proposed model agree very closely with the benchmark solutions.

For comparison, Figures 13(a) and (b) also gives the computations from the Power-law scheme. The results from the Power-law scheme on the coarse and fine grids illustrate significant discrepancy from the benchmark data, although on the finest grid, the results are almost identical with that from the proposed model.

The streamline patterns from the finest grid are presented in Figure 14 for $Re = 100$ and 1000. These results are quite similar to those of Demirdzic *et al.* [34].

5. CONCLUSIONS

In this study, a two-dimensional numerical model for incompressible fluid flows has been developed in boundary-fitted curvilinear coordinates with a collocated grid arrangement. An efficient fractional two-step implicit algorithm has been described in detail. The derivation is simple and straightforward. An implicitness coefficient Π is introduced to accelerate the rate

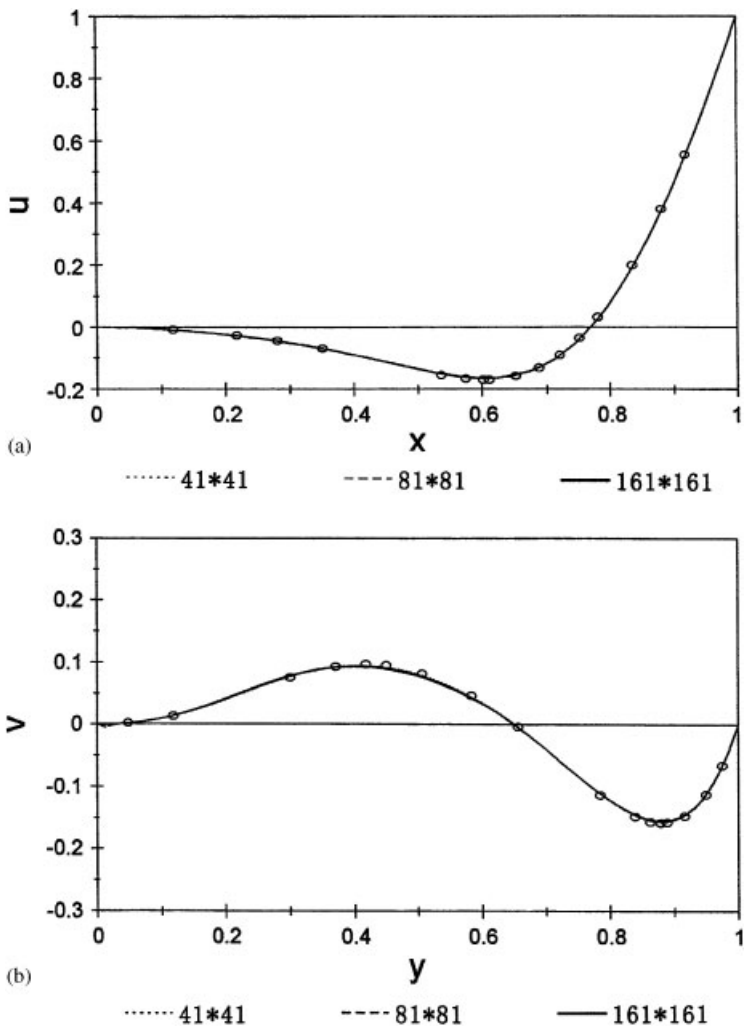

Figure 12. (a) Velocity profile (u) along CL1 against grid density for $Re = 100$; and (b) velocity profile (v) along CL2 against grid density for $Re = 100$.

of convergence. The final formulas are similar to that in the pressure correction procedure, i.e. the well-known SIMPLEC method could be considered as a special case of the proposed fractional two-step implicit algorithm (when $\Pi = 1$). In other words, the proposed algorithm links the fractional step method to the pressure correction procedure.

Three typical test cases have been selected, i.e. a pure convection problem, and two laminar separating flows. The performance of the proposed algorithm has been studied systematically by sensitivity analyses of the efficiency, accuracy, grid density, grid skewness and Reynolds number on the solutions.

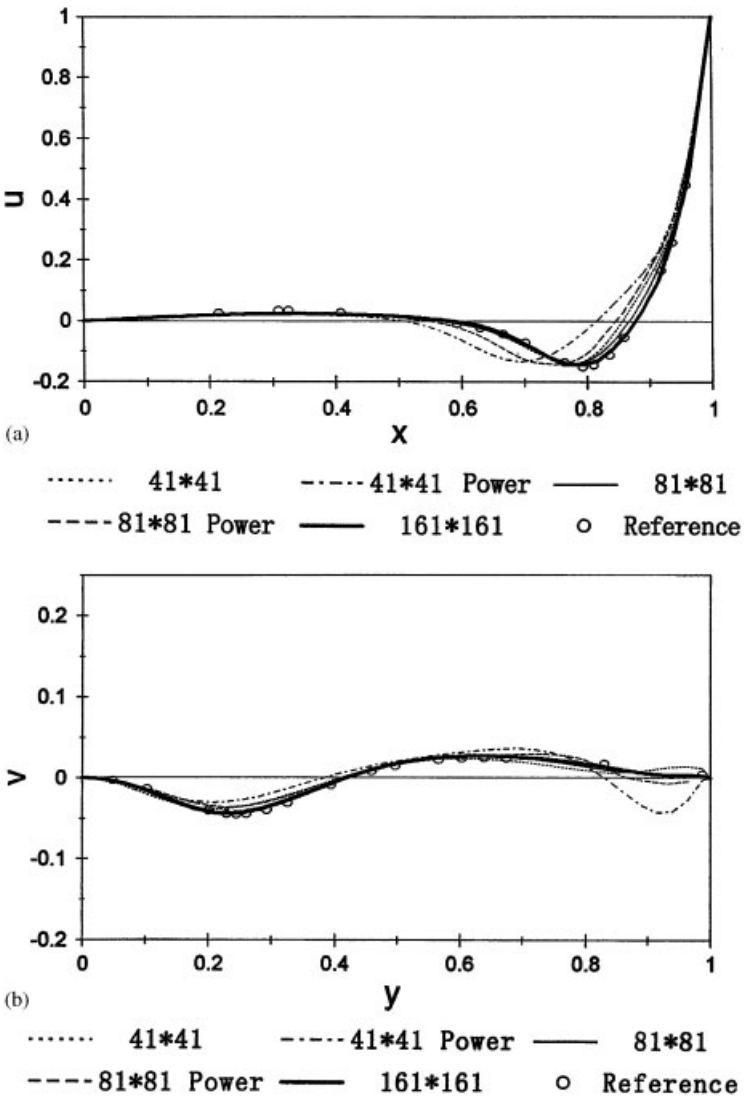

Figure 13. (a) Velocity profile (u) along CL1 against grid density for $Re = 1000$; and (b) velocity profile (v) along CL2 against grid density for $Re = 1000$.

The proposed algorithm significantly reduces the CPU cost at the optimal Π compared with that of the SIMPLEC method, e.g. 30–40% less CPU time in Case 2. Also the computational effort for convergence declines continuously over a broader range of time step at the optimal Π. The optimal Π varies typically in the range of 0.75–1 depending on the problems solved.

Studies also demonstrate that the solutions are relatively insensitive to grid skewness. As shown in Cases 2 and 3, simulations on various skewed grids predict either virtually the same results and/or in good agreement with other's data.

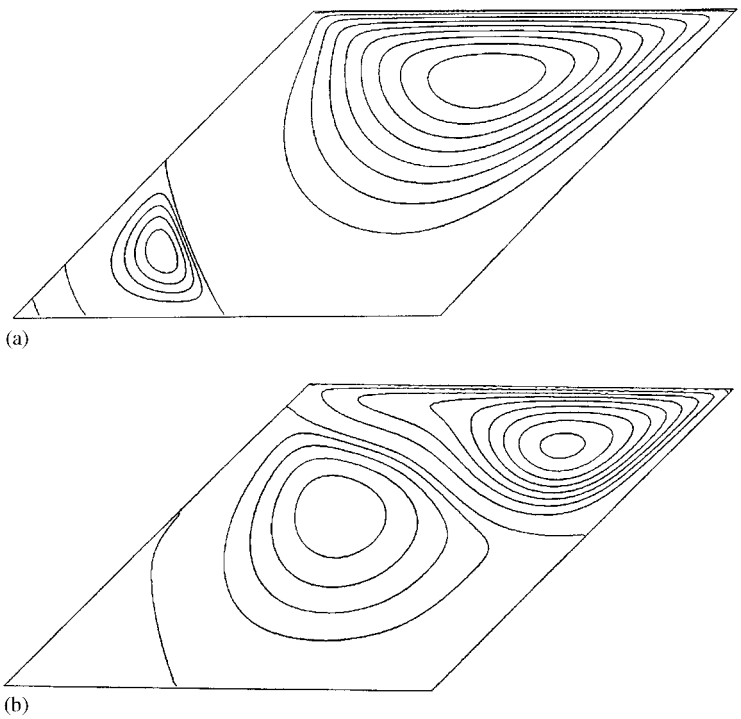

Figure 14. Predicted streamlines for: (a) $Re = 100$; and (b) $Re = 1000$.

Although the second-order upwind Roe's scheme has been used, other higher-order schemes can also been incorporated for discretization of the convective terms to minimize the possible numerical diffusion. As a reference, some computations in cooperated with the first-order scheme are included for comparison. As shown in the applications, simulations with the Power-law scheme present poor performance on relative coarse grids. This indicates that the first-order schemes may fail to give reliable solutions in the cases of high Reynolds number recirculation flow with a relatively coarse size grid due to high numerical diffusion. This conclusion is consistent with that of Tamamidis and Assanis [12].

Numerical tests have demonstrated that the proposed two-dimensional model is efficient and robust. Currently, this method is being applied to problems with complex physical domains, and has been extended to three-dimensional turbulent flows and mass transport [8, 24–26].

ACKNOWLEDGEMENTS

This research was supported by (1) the Great Lakes Institute for Environmental Research, University of Windsor, Canada, (2) the Natural Science and Engineering Research Council of Canada and (3) Managed- Programs LLC, Michigan, U.S.A.

REFERENCES

1. Thompson JF. Numerical solution of flow problems using body-fitted coordinate systems. In *Computational Fluid Dynamics*, Kollmann W (ed.). Hemisphere: New York, 1980.

2. Rodi W, Majumdar S, Schonung B. Finite volume methods for two-dimensional incompressible flows with complex boundaries. *Computer Methods in Applied Mechanics and Engineering* 1989; **75**:369–392.
3. He P, Salcudean M. A numerical method for 3D viscous incompressible flows using non-orthogonal grids. *International Journal for Numerical Methods in Fluids* 1994; **18**:449–469.
4. Patankar SV. *Numerical Heat Transfer and Fluid Flow*. Hemisphere, New York, 1980.
5. Rhie CM, Chow WL. A numerical study of the turbulent flow past an isolated airfoil with trailing-edge separation. *AIAA Journal* 1983; **21**:1525–1532.
6. Peric M, Kessler R, Scheuerer G. Comparison of finite-volume numerical methods with staggered and collocated grids. *Computational Fluids* 1988; **21**:435–454.
7. Majumdar M. Role of underrelaxation in momentum interpolation for calculation of flow with non-staggered grids. *Numerical Heat Transfer* 1988; **13**:125–132.
8. Ye J, McCorquodale JA. Three dimensional numerical modeling of mass transport in curved channels. *Canadian Journal of Civil Engineering* 1997; **24**(4):471–479.
9. Leonard BP, Dromond DJ. Why you should not use hybrid, power-law or related exponential schemes for convective modelling—there are much better alternatives. *International Journal for Numerical Methods in Fluids* 1995; **20**:421–442.
10. Leonard BP. A stable and accurate convective modeling procedure based on quadratic upstream interpolation. *Computer Methods in Applied Mechanics and Engineering* 1979; **19**:59–98.
11. Sweby PK. High resolution schemes using flux limiters for hyperbolic conservation laws. *SIAM Journal on Numerical Analysis* 1984; **21**:995–1001.
12. Tamamidis P, Assanis DN. Evaluation of various high-order-accuracy schemes with and without flux limiters. *International Journal for Numerical Methods in Fluids* 1993; **16**:931–948.
13. Roe PL. Approximate Riemann solvers, parameter vectors, and difference schemes. *Journal of Computational Physics* 1981; **43**(2):357–372.
14. Gaskell PC, Lau ABC. Curvature-compensated convective transport: SMART, a new boundedness preserving transport algorithm. *International Journal for Numerical Methods in Fluids* 1988; **8**:617–635.
15. Botella O. A high-order mass-lumping procedure for B-spline collocation method with application to incompressible flow simulations. *International Journal for Numerical Methods in Fluids* 2003; **41**(12): 1295–1318.
16. Erduran KS, Kutija V, Hewet CJM. Performance of finite volume solutions to the shallow water equations with shock-capturing schemes. *International Journal for Numerical Methods in Fluids* 2002; **40**(10):1237–1273.
17. Ye J, McCorquodale JA. Depth-averaged hydrodynamic model in curvilinear collocated grid. *Journal of Hydraulic Engineering* (ASCE) 1997; **123**(5):380–388.
18. Peric M. Analysis of pressure–velocity coupling on non-orthogonal grids. *Numerical Heat Transfer B* 1990; **17**:63–82.
19. Lehnhäuser T, Schäfer M. Efficient discretization of pressure–correction equations on non-orthogonal grids. *International Journal for Numerical Methods in Fluids* 2003; **42**(2):211–231.
20. Vuik C, Saghir A, Boerstoel GP. The Krylov accelerated SIMPLE (R) method for flow problems in industrial furnaces. *International Journal for Numerical Methods in Fluids* 2000; **33**(7):1027–1040.
21. Yanenko NN. *The Method of Fractional Steps*. Springer: New York, 1971.
22. Benque JP, Cunge JA, Feuillet J, Hauguel A, Holly FM. A new method for tidal current computation. *Journal of Waterway, Port, Coastal and Ocean Division* (ASCE) 1982; **108**(3):396–417.
23. Ye J, Dou G. Computation of incompressible fluid flows by an implicit fractional step scheme. *Proceeding of 2nd International Conference on Hydraulic and Environmental Modelling of Coastal, Estuarine and River Waters*, Bradford, England, 1992; 529–539.
24. Ye J, McCorquodale JA. Simulation of open channel flows by 3D hydrodynamic model. *Journal of Hydraulic Engineering* (ASCE) 1998; **124**(7):687–698.
25. Ye J, McCorquodale JA, Barron RM. A three-dimensional hydrodynamic model in curvilinear coordinates with collocated grid. *International Journal for Numerical Methods in Fluids* 1998; **28**(7):1109–1134.
26. Armaly BF, Durst F, Pereira JCF, Schonung B. Experimental and theoretical investigation of backward-facing step flow. *Journal of Fluid Mechanics* 1983; **127**:473–496.
27. Williams PT, Baker AJ. Incompressible computational fluid dynamics and the continuity constraint methods for the three-dimensional Navier–Stokes equations. *Numerical Heat Transfer B* 1996; **29**(2):137–273.
28. Guj G, Stella F. Numerical solutions of high-Re recirculating flows in vorticity–velocity form. *International Journal for Numerical Methods in Fluids* 1988; **8**:405–416.
29. Gartling DK. A test problem for outflow boundary conditions—flow over a backward-facing step. *International Journal for Numerical Methods in Fluids* 1990; **11**:953–967.
30. Barton LE. A numerical study of flow over a confined backward-facing step. *International Journal for Numerical Methods in Fluids* 1995; **21**:653–665.
31. Demirdzic I, Lilek Z, Peric M. Fluid flow and heat transfer test problems for non-orthogonal grids: benchmark solutions. *International Journal for Numerical Methods in Fluids* 1992; **15**:329–354.

32. Lin SY, Wu TM. An adaptive multigrid finite-volume scheme for incompressible Navier–Stokes equations. *International Journal for Numerical Methods in Fluids* 1993; **17**:687–710.
33. Davidson L. A pressure correction method for unstructured meshes with arbitrary control volumes. *International Journal for Numerical Methods in Fluids* 1996; **22**:265–281.
34. Oosterlee CW, Wesseling P, Segal A, Brakkee E. Benchmark solutions for the incompressible Navier–Stokes equations in general coordinates on staggered grids. *International Journal for Numerical Methods in Fluids* 1993; **17**:301–321.
35. Sheu TWH, Lee SM. A segregated solution algorithm for incompressible flows in general coordinates. *International Journal for Numerical Methods in Fluids* 1996; **22**(6):515–548.
36. Van Doormaal JP, Raithby GD. Enhancements of the SIMPLE method for predicting incompressible fluid flows. *Numerical Heat Transfer* 1984; **7**:147–163.

